FAB10: a user-oriented bandwidth-tunable extreme ultraviolet lightsource for investigations of femtosecond to attosecond dynamics in gas and condensed phases

D. Bresteau, C. Spezzani, O. Tcherbakoff, J.-F. Hergott, F. Lepetit, P. D'oliveira, P. Salières, R. Géneaux, M. Luttmann, I. Vadillo-Torre, et al.

FAB10: A user-oriented bandwidth-tunable extreme ultraviolet lightsource for investigations of femtosecond to attosecond dynamics in gas and condensed phases

D. Bresteau[1*], C. Spezzani[2], O. Tcherbakoff[1], J.-F. Hergott[1], F. Lepetit[1], P. D'Oliveira[1], P. Salières[1], R. Géneaux[1], M. Luttmann[1], I. Vadillo Torre[1], J. Lenfant[1], S. J. Weber[8], M. Dehlinger[3], E. Meltchakov[3], F. Delmotte[3], C. Bourassin-Bouchet[3], J. Im[3], Z. Chen[4], J. Caillaux[4], J. Zhang[4], M. Marsi[4], L. Barreau[5], L. Poisson[5], D. Dowek[5], M. Fanciulli[7], O. Heckmann[7], M. C. Richter[7], K. Hricovini[7], M. Sebdaoui[6], D. Dennetiere[6], F. Polack[6] and T. Ruchon[1*]

[1*]Université Paris-Saclay, CEA, CNRS, LIDYL, Gif-sur-Yvette, 91191, France.
[2]Elettra Sincrotrone Trieste, Trieste, Italy.
[3]Université Paris-Saclay, Institut d'Optique Graduate School, CNRS, Laboratoire Charles Fabry, Palaiseau, 91127, France.
[4]Université Paris-Saclay, CNRS, Laboratoire de Physique des Solides, Orsay, F-91405, France.
[5]Université Paris-Saclay, CNRS, Institut des Sciences Moléculaires d'Orsay, Orsay, 91405, France.
[6]Synchrotron SOLEIL, L'Orme des Merisiers, Gif sur Yvette Cedex, BP 48, 91192, France.
[7]Laboratoire de Physique des Matériaux et Surfaces, CY Cergy Paris Université, Cergy-Pontoise, 95031, France.
[8]CEMES-CNRS, Université de Toulouse, 29 rue Jeanne Marvig, Toulouse, 31055, France.

*Corresponding author(s). E-mail(s): david.bresteau@cea.fr; thierry.ruchon@cea.fr;

Abstract

We present the commissioning of the FAB10 beamline (Femtosecond to Attosecond Beamline at 10 kHz repetition rate) that has been developped and operated in the last few years at the ATTOLab facility of Paris-Saclay University. Based on the high harmonic generation process, the beamline is dedicated to investigations of ultrafast dynamics in a broad variety of systems ranging from gas phase to condensed matter in pump-probe arrangements. Its design and operation has been strongly influenced by both the laser and the large scale instruments communities, which makes it unique in several aspects. In particular, it is possible to tune the extreme ultraviolet (XUV, 10 - 100 eV) bandwidth from 0.2 to 20 eV - with corresponding pulse duration from 30 to 0.3 femtoseconds (fs) - thanks to an original and fully automated XUV spectral filter with three operation modes. After a general overview of the beamline features, each of those operation modes is described, characterized and illustrated with commissioning experiments.

Keywords: attosecond beamline, ultrafast dynamics

1 INTRODUCTION

High-order Harmonic Generation (HHG) phenomenon, observed by focusing an intense, ultrashort infrared (IR) laser into a gas target, allows the production of coherent XUV radiation with a tabletop setup [1, 2]. These HHG-based XUV sources find a complementary place alongside much larger scale sources such as synchrotrons and free electron lasers (FEL) that emit in the same wavelength range. They are relatively more affordable, and offer unique features, funnelling an increasing interest of the gas-phase and condensed matter research communities.

Whereas synchrotron instruments deliver high intensity over a very broad range of wavelengths, ranging from the IR to the hard X rays, they offer limited temporal resolution, in the hundred femtosecond range at best [3–5]. Past and current FEL facilities, emitting in the XUV spectral range, allowed to reach femtosecond time resolution with high intensity on target. However, the intrinsic time jitter of the source makes it difficult to observe subfemtosecond dynamics, and only recently was the generation of attosecond pulses at FELs demonstrated [6, 7]. New generation FEL sources, which are less than a handful worldwide, are currently passing this gap, at the price of severe pressure on beamtime [8]. On the other hand, XUV radiation sources based on HHG offer, at the cost of a lower intensity, unique features in terms of spatial and spectral coherences, time jitter, compactness and flexibility [9]. These characteristics makes them a source of choice to study ultrafast dynamics on the attosecond to few femtosecond timescale. Furthermore, the relatively low cost of the technique is not only an economical argument but also practically allows for dedicating longer beamtime to a project, which allows high risk-high reward strategies.

However, HHG sources are still in their infancy in terms of reliability, integration, and user-oriented experience, in comparison with large-scale instruments. Recently, following the example of FEL and synchrotron sources, a few HHG-based facilities were launched, e.g. ELI-ALPS in Hungary [10] or the Artemis facility in the UK [11], to cite a few. They are organized with specialized teams dedicated to the laser, the beamlines and the technical support, with the ambition to minimize the downtimes. Here we present FAB10 (Femtosecond-Attosecond Beamline at 10 kHz), one of the two first beamlines of ATTOLab, a French medium-scale facility. Its early design, including the planification of a new building, started in 2012, with the first commissioning users hosted in 2017, and a reliable commissioned use secured in 2021. It was designed through an integrated approach of several communities: a large panel of interested users from the gas phase and condensed matter communities orienting its capabilities at an early stage; a strong partnership with engineers and technical teams from SOLEIL synchrotron, and a coordination team from the HHG and attosecond community.

The users roadmap driving the design of FAB10 clearly pointed out towards two desired features: 1) the need for attosecond time resolution, which requires several eVs of bandwidth, and 2) spectrally narrow XUV pulses, of intrinsically longer (femtosecond) temporal duration, which would allow to disentangle different photoionization channels. One of the driving idea for the design of the beamline has been to offer such flexibility with the same source, on the same machine and on the same sample. It was finally designed with three operating modes, with bandwidths ranging from 100 meV to tens of eVs. A second clear requirement was to get an excellent vacuum, in the 10^{-10} mbar range, at the user's free port. This second requirement is particularly compelling for an HHG-based source, which typically runs with a first HHG chamber with 10^{-3} mbar residual pressure, and had strong impact on the design.

The paper is organized as follows: Sec. 2 is dedicated to the description and characterization of the laser system. After a general overview of the beamline (Sec. 3), we enter into a detailed description and illustration of the three branches of the beamline (Sec. 4).

2 LASER SYSTEM

The FAB1/10 laser system has been developed by Amplitude Technologies in collaboration with CEA Paris-Saclay, including specific developments performed within their joint laboratory Impulse. Based on chirped pulse amplification [12], a specific 10 kHz front-end is used to seed two separate amplification lines respectively at 1 and 10 kHz. A global sketch of the system is displayed in Fig. 1.

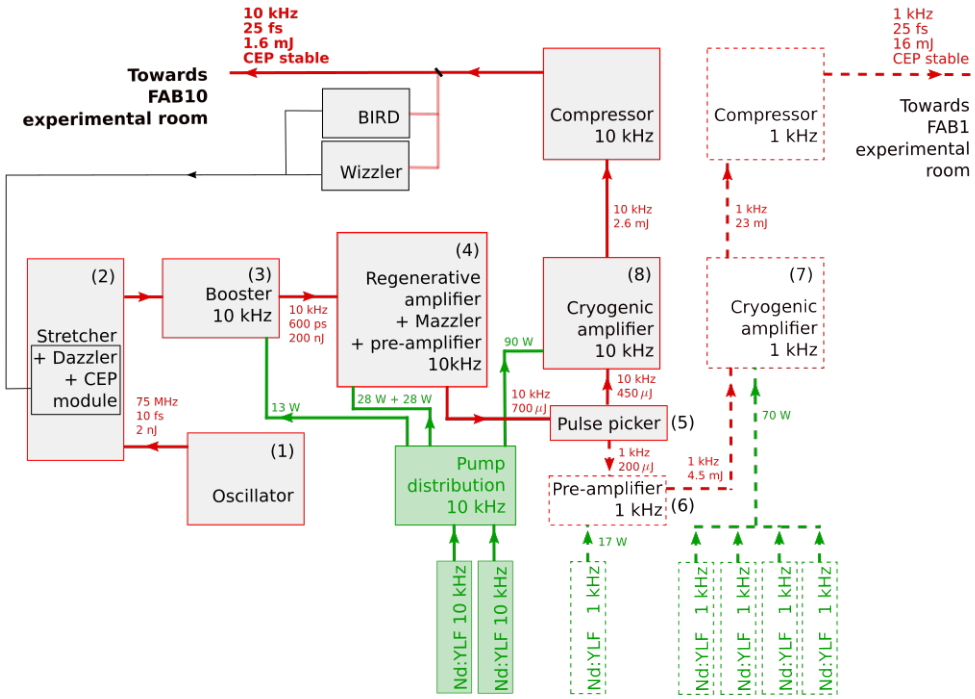

Fig. 1 FAB1/10 laser system overview. The dashed blocks are related to the 1 kHz part of the system, which are not directly relevant for this work.

2.1 Front-end

The front-end is seeded by a carrier-envelope phase (CEP) stable Kerr-lens mode locked Ti:Sa oscillator (Rainbow CEP4, Femtolaser) (1) (see numbered parts in Fig. 1) delivering at a 75 MHz repetition rate, 200 mW, sub-10 fs pulses with a spectrum extending from 640 to 940 nm at the edges. The CEP control is based on the feed forward technique [13], yielding a residual theoretical CEP noise well below 50 mrad. A grating-based (1200 grooves/mm) stretcher (2) with 150 nm spectral bandwidth throughput in an all-reflective aberration-free Offner-triplet configuration [14] temporally extends the pulses with a stretching factor of 5 ps/nm. The stretched pulse duration (600 ps full width at half maximum (FWHM)) allows for high amplification while keeping a low B-integral value. The stretcher has been optimized to ensure a low sensitivity to vibrations, thus limiting the deterioration of the CEP stabilization in this highly dispersive element [15]. An acousto-optical programmable dispersive filter (AOPDF, Dazzler from Fastlite) is placed at the output of the stretcher [16]. This device, which allows spectral beam shaping in amplitude and phase, is coupled to a temporal pulse characterization device located downstream each final compressor of the laser system. At this output, a small portion of the beam is extracted, in the range of a few tens of μJ, and directed to the entrance of a Wizzler (Fastlite) or SHG-FROG (Femtoeasy) device to retrieve the pulse temporal profile. The settings of the AOPDF are then adjusted to compensate the residual spectral dispersion terms in order to achieve the shortest pulse duration. On the same diagnostic line, we have also installed an f-2f interferometer based on an analogical detection (BIRD, developped with Amplitude Technologies) to measure the CEP drift and to send the correction signal to the Dazzler. Thus, the integration of the AOPDF in these two loops ensure both an optimal pulse duration and CEP slow drift correction.

After the dispersive filter, the beam is sent to a six-pass ring-amplifier (3) to boost the pulse energy in the hundred nJ range while keeping the 150 nm spectral bandwidth. It is pumped at 10 kHz by 13 W of a Q-switched frequency doubled Nd:YLF laser at 532 nm (MESA Continuum lasers). A KD*P Pockels cell between the

first three and the last three passes decreases the repetition rate from 75 MHz to 10 kHz. The ring configuration of this multipass amplifier, or booster, ensures small angles and good overlap between each pass and the pump inside the Ti:Sa crystal; allowing an overall gain of 100, and leading to an IR pulse energy of roughly 200 nJ. This enhanced seed energy helps to obtain a good contrast between the picosecond and the nanosecond regime after the regenerative amplification cavity (4) used downstream. It includes two Brewster-cut Ti:Sa crystals, and two KD*P Pockels cells as injection and extraction devices. Compared to standard designs, this original W-like designed water-cooled cavity enables a better heat load and thermal lensing management that generally limit the cavity efficiency and lower the beam quality [17]. To counteract the gain narrowing effect [18], an intracavity programmable filter (AOPGCF or Mazzler) [19] is inserted in the cavity. Spectral losses are created where the spectral gain is higher, leading to an amplification enhancement at the edges, and a final homogeneous amplified spectrum. Pumped with a total power of 27 W, this double-Ti:Sa-crystal cavity could generate pulses up to 5.1 W (0.3 % RMS stability) in a moderate spectral bandwidth, i.e., 50 nm at $1/e^2$. Routinely, when AOPGCF is implemented and after an optimization process, an amplified spectrum with 85 nm at $1/e^2$ is obtained with an output power of 3.5 W (0.3 % RMS stability) for 28.5 W of pump power. Using the system at its limits, the spectral width is increased up to 110 nm at $1/e^2$ with an energy reaching 2.5 W. Further amplification up to 7 W (0.35 % RMS stability) is achieved in a two-crystal single-pass amplifier (10 kHz preamplifier) pumped between 25 and 28 W (MESA HP Continuum) depending on the pulse spectral width. Since the single-pass amplifier is also affected by gain narrowing and red-shifting of the amplified pulse, the spectral shaping by the Mazzler is performed using the output spectrum of the preamplifier. The gain narrowing pre-compensation ensures that the spectrum at the output of the preamplifier has the desirable width and shape for a pulse duration as short as possible. For the pumping scheme of all amplifiers, dichroic mirrors have been used to ensure high transmission at the pump wavelength and high reflectivity at the IR wavelength. The 10 kHz front-end output finally seeds

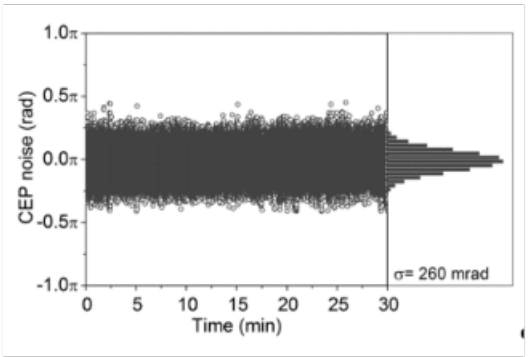

Fig. 2 FAB10 laser shot-to-shot residual CEP noise measurement recorded over 30 minutes with a standard deviation of $\sigma = 260$ mrad. Figure extracted from [20].

two high-energy amplifiers; one at 1 kHz and the second at 10 kHz [20].

2.2 High energy amplification

30 % of the front-end output energy (200 μJ per pulse) is used for the 1 kHz beamline, which we describe briefly here for the sake of completeness. This fraction of the energy is sent to a KD*P Pockels cell (5) to reduce the pulse repetition rate from 10 kHz to 1 kHz. A water-cooled 5-pass butterfly pre-amplifier (6) amplifies those pulses up to 4.5 mJ with 17 W of pump (Thales Jade 2). A final 4-pass butterfly cryo-cooled amplifier (7) (T = −130°C) boosts the energy up to 23 W with 70 W of pump power (two Jade 2 Thales and one double TERRA from Continuum).

The remaining 70 % of the output energy from the 10 kHz front-end, corresponding to 450 μJ, is seeded in the 10 kHz cryo-cooled main amplifier (8). Similarly to the 1 kHz high-energy amplifier, the Brewster cut Ti:Sa crystal of this last amplifier stage is cooled down to −150°C under vacuum with a vibration-free cryogenic cooler to counteract thermal lensing. The amplifier does not reach full saturation condition compared to the 1 kHz one and it is thus more sensitive to the injected power, leading to 26 W (90 W pump power MESA HP) when seeded by pulses with 85 nm spectral width at $1/e^2$. An expansion telescope, identical on both amplification lines, increases the beam size to 35 mm at $1/e^2$ in order to set the power density in the compressor optics below 3 W/cm^2. The amplified laser beams at 1/10 kHz are sent to

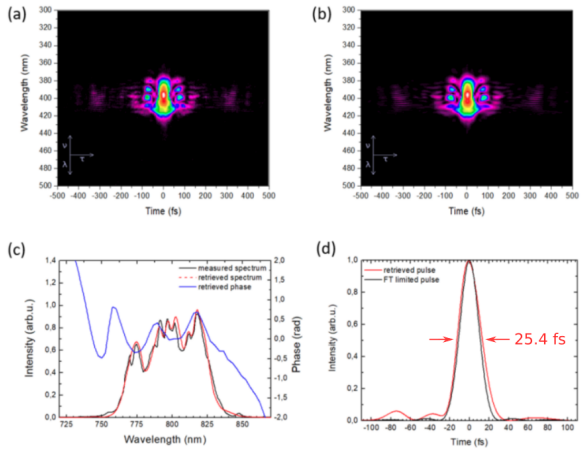

Fig. 3 FAB10 laser pulse measurement with single shot SHG-FROG device. (a) Measured SHG-FROG trace. (b) Retrieved SHG-FROG trace. (c) Retrieved spectrum (red line) and phase (blue line) compared with the experimental measured pulse spectrum (black line). (d) Retrieved intensity profile (red curve) superimposed with the Fourier-Transform limited pulse (black curve). The Fourier-limited duration is 24 fs.

a CEP-compatible reflection grating-based compressor located in separate experimental rooms after 3 meters of free propagation. The beam pointing of each line is stabilized thanks to two motorized mirrors at the output of the cryo-cooled amplifiers coupled to a correction loop based on near field and far field imaging of the output beam.

2.3 Compression, CEP stabilization and performances

To prevent our systems from being critically sensitive to mechanical vibrations, and also considering the extended beam dimension, special tuning-free CEP-compatible grating mounts have been designed for the compressor to ensure a robust and stable support for the optics. Associated to a controlled environment with smooth air flow and a regulated room temperature within $\pm 0.5°C$, the correction loop allows to reach a beam pointing stability of 4 μrad RMS. Those conditions are also of prime importance to reach the best CEP stabilization of the amplified pulses. When the CEP correction loop is applied on the Dazzler after measurement with an analogical BIRD device [21], the remaining shot to shot CEP noise is 340 mrad at 1 kHz and 260 mrad at 10 kHz, as shown in Fig. 2. The difference is mainly due to the fact that a higher repetition rate offers a larger correction bandwidth. The compressors are in a double-pass Treacy configuration using 1480 grooves/mm gratings. The use of different groove density gratings in the stretcher and the compressor results in a better compensation of the material dispersion, specifically for the fourth order spectral dispersion term in addition to the AOPDF [22]. Their transmission efficiency of about 70 % leads to 16 mJ and 1.6 mJ pulses respectively at 1 kHz and 10 kHz. The RMS shot to shot energy stability is around 0.8 % and 1.1 % respectively. A pulse duration of 25 fs is achieved routinely on each line after a Wizzler-Dazzler spectral phase flattering loop as shown on Fig. 3. One has to note that the dispersion compensation loop is performed on one amplified line for both lines simultaneously. However, the pulse compression default compared to optimum compression is then less than 1 fs on the other line.

The 16 mJ, 25 fs output at 1 kHz is sent towards the FAB1 beamline and experimental room, which have been described elsewhere [23] [24]. The 1.6 mJ, 25 fs output at 10 kHz is used in the beamline described in the remaining of this paper.

3 BEAMLINE OVERVIEW

3.1 Beamline environment

The laboratory is built on the very thick concrete structure of the former linear accelerator at CEA Saclay and thus benefits from a high mechanical stability, of VC-E grade. The beamline is hosted in a clean room environment (ISO 8 grade) with temperature ($22 \pm 1\,°C$) and humidity control ($< 55\,\%$) all over the year. All sources of mechanical noise, such as primary pumps and power supplies, have been deported into neighbouring isophonic service rooms, and placed on massive concrete platforms placed on silent blocks. The laser room is maintained at a 10 mbar overpressure compared to the experimental rooms, which are themselves at 10 mbar over the atmospheric pressure. This results in high reproducibility and long-term stability of the optical setup. Service water is maintained at $15 \pm 0.5\,°C$ in a closed loop circuit. The water is filtered and passes through a water softening system to prevent clogging. The building is fully equipped to use toxic gases. Its detectors are linked to a gas central control alarm

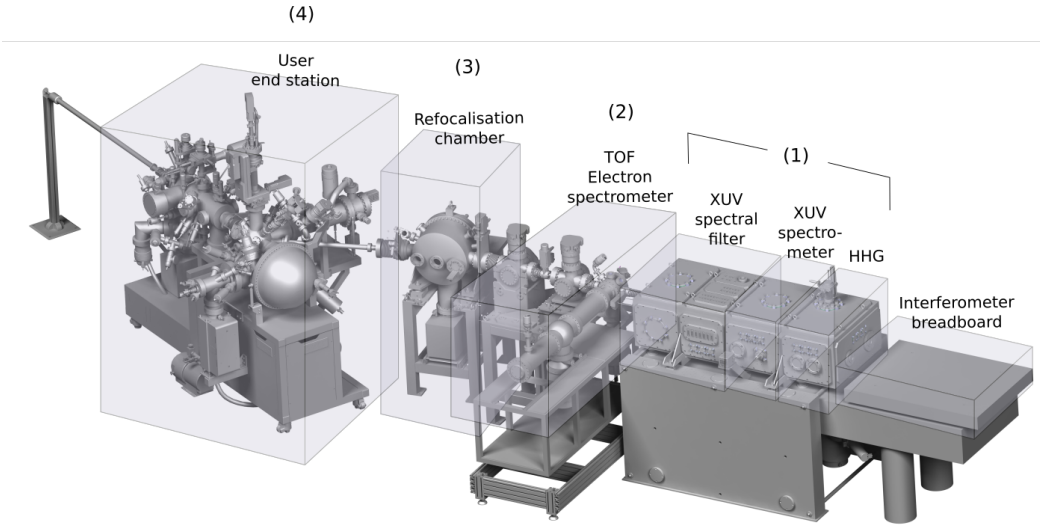

Fig. 4 FAB10 beamline overview. The numbering corresponds to the vacuum system blocks (see text).

block, directly linked to the CEA fire brigade. Specific certified gas lines with low rugosity are installed to drive the gas from either an external storage room, or an hermetically sealed certified cabinet for bottles smaller than 10 liters.

3.2 Vacuum system

The vacuum system is split in four blocks (see Fig. 4): (1) the HHG generation chamber up to XUV spectral filter, (2) time-of-flight (TOF) electron spectrometer, (3) differential pumping and refocalisation chamber and (4) the user end station. Each of them can be isolated from the rest of the vacuum system, which allows one to vent or pump independently any of those blocks. Two root pumps are dedicated to the beamline and user blocks respectively. The former is backing 8 turbomolecular pumps protected by computer-controlled gate and angle valves on each side. All pumps and valves are controlled by a home-made control-command program, which monitors 9 pressure gauges and is able to protect the installation in case of detected default.

In normal operation, the pressure in the HHG chamber is a few 10^{-3} mbar. It is only connected to the following chamber by a skimmer with a 2 mm hole, ensuring a good differential pumping. In regular operation, a pressure of a few 10^{-6} mbar is obtained in the following compartment.

This compartment is connected through a KF40 flange to the TOF. Gas may be injected by a needle in the active region of the TOF, leading to a backing pressure of a few 10^{-4} mbar in the head of the TOF in regular operation. A differential pumping between the TOF and the following chamber is ensured by a metallic cylinder, 10 cm long and 4 mm in diameter, placed a few centimeters after the TOF focus.

The final compartment, block (3), is pumped by two turbomolecular pumps (400 l/s), located close to the exit of the differential pumping cylinder, an ionic pump, and one last turbomolecular pump close to the user's free port. It is designed for baking up to 120 °C. With this arrangement, we can offer ultrahigh vacuum conditions (10^{-10} mbar) to users in steady operation.

This pumping system is a major source of vibrations. All blocks have been precisely positioned by SOLEIL alignment group, before being permanently sealed in the ground. In addition, around the most sensitive part which wraps the optical interferometer, i.e. block (1), heavy tanks filled with specific crushed sand ($\simeq 1$ ton each), are holding the vacuum chamber and pumps to absorb their vibrations. The optical breadboard placed in this tank is directly connected to the optical table lying underneath, with only three bellow-type feed-through connectors. This optical table is common with the rest of the interferometer lying

in air, and very immune to the vacuum system vibrations due to this very limited connection.

3.3 Optical scheme

The key feature of the beamline is the ability to perform highly stable pump-probe experiments with tunable XUV pulse duration over two orders of magnitude. Its implementation consists of three optical XUV+IR interferometers, sketched in Fig. 5, whose core element is an XUV spectral filter. It consists of a 730 × 650 mm motorized breadboard, with micrometer positioning capabilities on the transverse horizontal axis, over which are mounted XUV optics defining three different optical paths. Switching from one branch to another thus mainly consists in translating this breadboard. Further details are given in Sec. 4.

The cornerstone of the narrow band (NB) path, which selects an XUV bandwidth in the 200 meV range, with corresponding femtosecond duration, is a conical diffraction monochromator that diffracts the XUV radiation in the vertical direction. The wavelength of interest is selected with thin slits inserted at the TOF focus. The apparatus is described in details in Sec. 4.2. As those thin slits would be destroyed by an intense IR beam, the IR beam of this interferometer is directed outside of this block towards a recombination mirror placed dowstream the refocusing unit. For femtosecond pump-probe experiment, the matching of the wavefronts of the pump and probe is of little importance. We thus implemented a non-collinear geometry thanks to a mirror placed inside the refocalisation chamber. The overall mechanical stability is sufficient to stand a time resolution of a few tens of femtoseconds, limited by the pulse duration at the output of the monochromator.

The very broadband (VBB) interferometer is more demanding in terms of mechanical stability since it transmits the broadest bandwidth (10's of eV). The recombination of the two beams is done with a drilled mirror in collinear geometry. This interferometer can be actively stabilized using the LIZARD technique [25] that has been demonstrated on this beamline.

The NB and VBB interferometers share a unique translation stage (DL, Fig. 5) to adjust the delay between the two beams (SmarAct double SLC-24150 [26]). It is based on slip-stick technology that allows nanometer precision over a range of 10 cm. The time zero of each interferometer is within this range, which makes it easy to switch from one branch to another.

The BB interferometer is by construction the one that provides the highest passive stability since the XUV and IR beams are split and delayed by a unique optical mount in a collinear geometry. In this configuration, the central part of the driving beam after the HHG step is absorbed by a dot aluminium filter of 4 mm diameter. Downstream this dot, we have an XUV plain beam confined near the propagation axis surrounded by an annular IR beam. Both are focused through reflection off a common XUV coated spherical mirror in quasi normal incidence, and further separately reflected by two concentric mirrors, whose longitudinal location may be adjusted by a similar SmarAct translation stage. The intensity of the IR pulse can be attenuated using an iris placed between the generation and the first reflection.

The optical elements are designed to have the XUV focus of all paths at the same location in the interaction region of the electron spectrometer. A toroidal mirror mounted in the refocusing chamber allows one to image the TOF focus at the user focus.

3.4 High harmonic generation

To drive high harmonic generation process, part of the laser beam (300 to 700 μJ) is focused by a 0.5 m focal length lens in a gas cell. The beam, which had been beforehand telescoped down to a waist of 20 mm, is typically irised down to 12 mm. We observed a beam radius at focus of 40 μm at $1/e^2$, close to the expected value for a perfect wavefront.

The generation cell is made of a 10 mm long metallic cylinder of 500 μm diameter. Argon gas is injected continuously through a hole in the center of the cylinder. Generation in neon has been observed using the XUV photon spectrometer, but the resulting flux is for now too low for applications. The generation conditions could probably be improved by using a longer focal length, but in the present setup such attempts led to destroying the aluminium filter positioned at 0.7 m from the source. Alternatively, removing this filter, we observed the formation of an alloy on the first flat

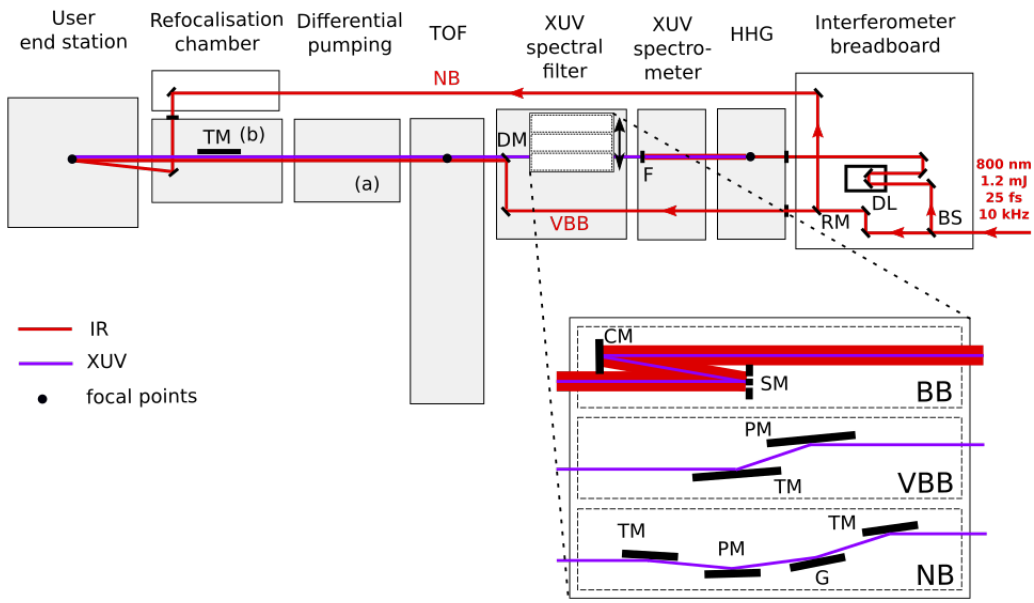

Fig. 5 FAB10 general optical scheme. The grey blocks represent under vacuum parts. BS: beam splitter (80% reflexion, 20% transmission), DL: delay line, RM: removable mirror (used in NB mode), F: metallic filter, DM: drilled mirror, CM: curved mirror, SM: split mirror, PM: plane mirror, TM: toroidal mirror, G: gratings. XUV flux measurements can be done by the help of an XUV photodiode in (a) or by measuring the photocurrent on the last toroidal mirror in (b) (Sec. 3.5.1).

gold mirror, ruining its reflectivity. The replacement of the flat gold mirror by a silica plate with an IR antireflection coating to discard much of the IR power before hitting the filter will be tested in the future to circumvent this difficulty.

3.5 Diagnostics

3.5.1 XUV flux and spatial profiles measurements

The XUV intensity can be measured using two diagnostics: (a) an XUV photodiode mounted on a translation stage can be inserted into the beam and (b) by the help of an electrical connector in contact with the surface of the toroidal mirror mounted in the refocusing chamber (Fig. 5). As the beam hits the mirror surface, photoelectrons are emitted from the gold atoms of the coating, which will induce an electrical current from the mass collected by the contact and measured by a picoamperemeter. The measurement is averaged over 10 rolling laser shots and continuously recorded together with a timestamp for further normalisation if required. This last method is the privileged one during acquisition, as it does not require to block the beam propagation.

The energies per pulse given in Table 1 are estimated using the following method. The current intensity measured through the mirror connector is given by:

$$I = q\sigma dN = \frac{q\sigma N}{\pi r^2} \tag{1}$$

with q the elementary charge of the electron, σ the photoionization cross-section of metallic gold (taken at a photon energy of 35 eV [29]), d the density of atoms at the surface of the mirror, r the atomic radius of gold, and N the number of photons per second. Taking a cross section of 45.5 Mbarn at 35 eV, a gold atomic radius of 1.44 Å, and for a reasonable value of 1 nA measured from the gold mirror, we found about 8×10^{10} photons per second and 50 pJ per pulse. It should be noticed that such a measurement corresponds to effective values at the user focus, except for one reflection on the refocusing mirror. The flux parameters that we measure may be compared to those from similar beamlines. For

Table 1 Summary of the main characteristics of the three branches.
The estimated or calculated values are indicated with a grey background, while the measured values are indicated with the associated uncertainty after the ± symbol.
The value of the bandwidth given corresponds to a raw estimation of the XUV filter bandwidth. The structure of the HHG spectrum has to be taken into account to get the bandwidth of the emission on target.
The pulse duration is given on target.
The photon flux is given for typical generation conditions with Argon, the standard deviation is calculated over several years of operation.
The passive stability values given correspond to long-term drifts of the interferometers. They have been measured by spectral interferometry, as close as possible to the experimental conditions. We notice that the interferometers are more stable after several hours of illumination, which tends to suspect thermal effects on mirrors as a major contribution to the instability.
APT: attosecond pulse train. RMS: root mean square. N/A: not available.

	bandwidth of the optical system (eV)	pulse duration (fs)	energy per pulse (pJ) photon flux (10^{10} photons/s)	pump-probe jitter passive stability active stability
VBB	100	0.3 ± 0.1 [a] in an APT	85 ± 48 15 ± 8	7.6 ± 0.1 fs/hour 0.028 ± 0.010 fs RMS[b]
BB_15eV	15	0.35 ± 0.05 [c] in a 11 ± 2 fs APT	7.5 ± 2.5 1.3 ± 0.4	4 ± 2 fs/hour N/A
BB_3eV	3	14 [d]	2.9 ± 0.8 0.52 ± 0.15	4 ± 2 fs/hour N/A
NB	0.2 - 1.6 [e]	30 [f]	3.7 ± 1.5 0.65 ± 0.28	14 ± 2 fs/hour N/A

[a] Measured with the RABBIT technique [27].
[b] This value corresponds to short-term jitter. This result has been obtained with the LIZARD active stabilization technique [25].
[c] The XUV pulse structure with the 15 eV bandwidth coating has been measured with the Mixed-FROG technique (see Sec. 4.3.2).
[d] This value is an estimation taken from the Mixed-FROG analysis on BB_15eV branch by isolating numerically H21.
[e] Theoretical values of the output bandwidth of the monochromator, which depends on the grating parameters (Table 2).
[f] This value is estimated from a similar system [28] and the minimal theoretical value of the pulse duration (Table 2).

example, the VBB branch of FAB10 is analogous to the HR GHHG beamline at ELI-ALPS, for which 50 pJ of XUV energy per pulse was reported [30]. This value is 40% less than what we measure (85 pJ), which is expected by the scaling of HHG with drivers wavelengths ($\lambda = 1030$ nm vs $\lambda = 800$ nm). As for the NB branch of FAB10, it compares to the 1 kHz beamline at Artemis facility. A monochromatized photon flux of 2×10^{10} photons per second is reported at 25 eV [31]. This result is three times more than what we measure on FAB10 (0.65×10^{10} photons per second at 35 eV). However, it should be noted that even for a 10 kHz repetition rate, this flux was exceeding the limit given by the appearance of space charge effect in both the COLTRIMS or ARPES setups.

Moreover, an XUV photon spectrometer can be inserted in the beam just after the HHG source. It consists in a grating (Shimadzu, 1200 grooves/mm, gold coated), mounted on a motorized translation stage. The XUV radiation is then focused on a stack of three microchannel plates followed by a phosphore screen, which is imaged by a camera outside the vacuum chamber. This instrument not only yields the spectrum of the emission, but also the spatial profiles of the harmonics in one direction. It thus allows to adjust the generating conditions to favour the short trajectories, and to yield close to Gaussian intensity profiles.

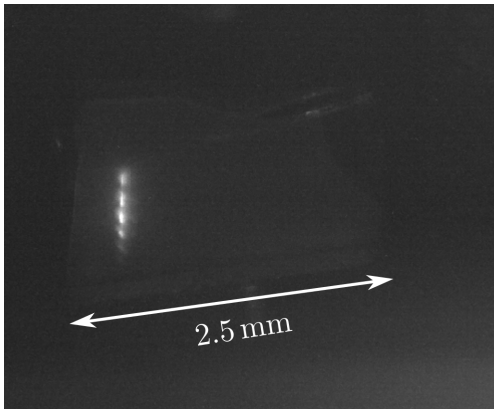

Fig. 6 Image of the scintillator crystal at the TOF focus. One can clearly see the vertical dispersion of the harmonics using the NB branch.

Finally, a YAG:Ce crystal (CRYTUR [32]) can be inserted at the TOF focus to image the XUV beam profile (Fig. 6).

3.5.2 TOF electron spectrometer

The magnetic bottle time of flight electron spectrometer is permanently installed on the beamline. It can be used in combination with the BB and VBB branches.

It is composed of an electromagnet surrounding the source of photoelectrons to collect them at the entrance of a 1.4 m drift tube. Another coil guides them through the tube up to microchannel plates that amplify the electronic signal, detected on a 1GHz bandwidth oscilloscope, triggered by the laser pulse. The principles of the design can be found in [33].

The instrument is used to temporally characterize the XUV pulses that are produced at the output of the XUV spectral filter, with the RABBIT [27] or more advanced characterization techniques like Mixed-FROG [34]. Moreover, it can implement the LIZARD technique to actively stabilize the pump-probe delay at the attosecond time scale [25]. Finally, it can be used to host a reference experiment that is synchronized with the one at the user focus [35].

3.6 Control and acquisition programs

The home-designed computer programs that control the vacuum system, the positioning of the XUV spectral filter and the refocusing mirror have been written in Labview.

The acquisition programs, the active stabilization program and the TCP/IP communication with the users computers have been developed using PyMoDAQ, an open-source python framework for data acquisition programs [36]. This choice is dictated by the ease of implementation of future evolutions.

4 THE THREE BRANCHES OF THE BEAMLINE

Spectrally manipulating XUV HHG beams while maintaining their temporal properties close to the Fourier limit can be particularly challenging. The most common implementation relies on series of metallic filters of different compounds, inserted in the HHG generated beam, which select finite bandwidths. However, they offer limited flexibility and are notoriously fragile. Their use with high intensity lasers can lead to frequent need for replacement. Consequently, a different choice has been made for FAB10.

The XUV spectral filter (Fig. 7) implements three branches (VBB, NB, BB) introduced in Sec. 3.3, each with a different spectral acceptance. Their interchangeability is constrained by two fixed points, namely the positions of the HHG and TOF focuses (Fig. 4). Consequently, all three branches have the same horizontal offset between incoming and outgoing beams with a total null angular deviation, and have comparable numerical aperture. They are inserted at their respective working position using a transverse translation (CINEL [37]), whose repositioning reproducibility has been commissioned at SOLEIL Synchrotron. The main characteristics of the branches are summed up in Table 1.

4.1 Mechanical conception of the XUV spectral filter

The motorized breadboard and the monochromator grating support (NB branch) has been designed and manufactured by CINEL. All grazing-incidence optical mounts (Fig. 8) have been designed and characterized in the framework of a collaboration between CEA and SOLEIL synchrotron. The base of the mounts, which implements the pitch and translation movements, are

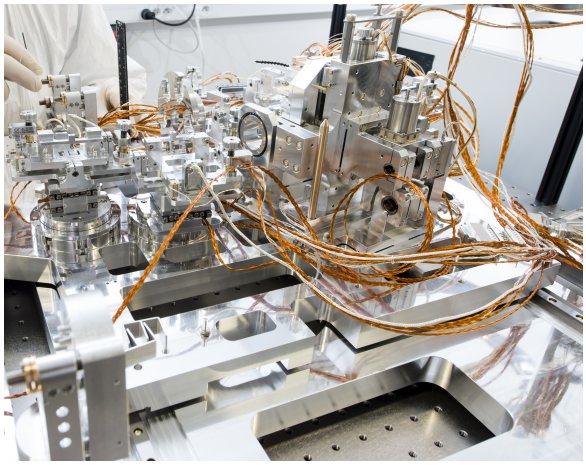

Fig. 7 The XUV spectral filter mechanics (without optics) outside the vacuum chamber.

made with SmarAct actuators. The roll and yaw rotations are driven with Physik Instrument piezo-actuator fine screws ending with a metal ball that pushes on a sapphire polished plate at the end of a lever. All motors are UHV compatible so as to prevent any contamination of the mirrors surfaces. The mechanical design principle was to get as small supports as can be with high frequency vibrational modes and low stress on the optical surfaces. The rotation axes have been designed to be as close to the optics surface as possible. All rotating movements have been designed using C-flex torsion bearings. The advantages are that they present no mechanical backlash out of their equilibrium point, high torque when in position, that no friction is required, and thus no lubricant. The movements are measured as close to the optical surfaces as possible with Mercury encoders. That combination results in great reproducibility, low hysteresis, and very limited friction when moving.

4.2 NB branch

The NB branch is designed for monochromatization of the XUV with sub-harmonic spectral resolution, typically 200 meV at 25 eV. Its optical scheme is shown in Fig. 9. It is composed of four optical elements, plus an horizontal slit that is inserted at the TOF focus (Fig. 5).

At wavelengths of a few tens of nanometers, it is usual to find grating monochromators [38, 39], but the specificity of FAB10 lying in the transport of short temporal pulses, the monochromator

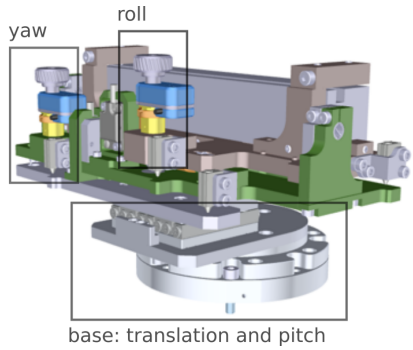

Fig. 8 Mechanical support of the VBB toroidal mirror (rear view).

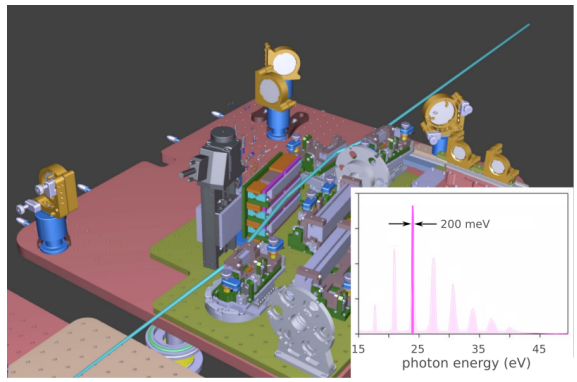

Fig. 9 The NB branch optical scheme. Inset: typical spectrum transmitted by the system.

has been inspired by a design published by L. Poletto for Artemis [40]. This design couples two toroidal mirrors in a pseudo-Wolter configuration, i. e. deviating in the same direction, with a grating in between, where the beam is collimated. The pseudo-Wolter configuration naturally leads to a plane mirror being added between the grating and the second toroidal one so that the Abbe [41] condition is satisfied. As diffraction stretches the duration of an incoming pulse, the choice here was to use as low a grating line density as possible. In order to maintain the resolution, a conical diffraction design is used here. The grooves of the grating and incoming wave vector are coplanar, which leads to diffraction orders spread along a circle in the selection slits plane instead of being spread along a line. Several fixed width slits (25 μm, 50 μm, 100 μm and 200 μm) are held by a small rod that can be inserted with a motorized translation in the TOF focus.

Since both source and image points are fixed for interchangeability purposes, the grating is

operated in a Littrow configuration, the energy being selected with a rotation of the grating around the tangential axis of the grating surface.

A few gratings have been purchased thus far, so as to adapt the resolution of the NB branch to the users' needs. The grating mount holds three gratings at a time so as to quickly adapt the resolution of the monochromator under vacuum. The list of gratings with their associated resolution is given in Table. 2. All gratings are blazed to maximize throughput at a given central wavelength.

Table 2 Theoretical values of the output bandwidth and minimal pulse duration of the NB branch [42] for the available gratings.

Grating	Optimal energy (eV)	Output bandwidth (eV)	Pulse duration (fs)
85G	15	0.19	36
100G	27	0.52	24
150G	41	0.79	23
158G	50	1.12	20
200G	27	0.26	47
300G	83	1.63	23

The number in the grating name corresponds to the number of grooves per millimeter. The output bandwidth value is calculated for a source diameter of 40 μm and an output slit width of 50 μm, at the optimal energy.

Applications of the NB branch

The NB branch is well suited for angle resolved photoemission spectroscopy (ARPES) on solids: it combines a reasonable energy resolution ($\sim$200 meV) and repetition rate (10 kHz) to produce data within a few tens of minutes. It provides an excellent time resolution of a few tens of femtoseconds which allows one to study the dynamics of excited states.

The main difficulty in performing ARPES on such a source resides in the proper handling of space charge effect. The XUV pulses produced tend to be too powerful. The numerous electrons ejected per shot from the sample in such a short time produce a broadening and a shifting of the measured spectra. For a sample with a high photoemission cross-section, the only way to prevent the phenomenon is to reduce the source fluence. With the specifications of the beamline, considering a spot size of 100 μm, the simple model

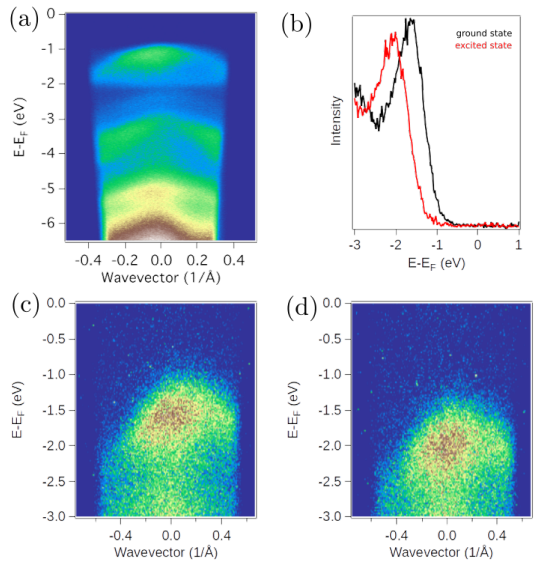

Fig. 10 (a) ARPES of InSe valence band states with a Helium lamp (photon energy = 21 eV). (b) Energy shift between the ground (in black) and excited state (in red). The energy distribution curves have been obtained by integrating the wavevector axis from the images in panel (c) and (d), respectively. (c) and (d) are ARPES images taken with the NB branch of FAB10 (H23, photon energy = 35.6 eV) from the sample in its ground state (c) and photoexcited with an 800 nm, 1 mJ/cm^2 pump beam at 200 fs time delay (d).

presented by Corder [43] states that the sample current should not go beyond 10 pA if we want to keep a spectral resolution around 100 meV.

As a typical example, we present in Fig. 10 the study of the valence band of an InSe sample. The sample is naturally n-doped. Its valence band states are presented in Fig. 10 (a), using a He lamp as excitation source and a scanning acquisition mode for the electron energy analyzer. In order to perform time-resolved scans, the measurements are performed with the detector at a certain fixed energy, as in Fig. 10 (c) and (d) using XUV photons from FAB10. The signal to noise level is sufficient to directly measure the energy-momentum $E(k)$ dispersion of the states at the top of valence band, with an acquisition time for each image of the order of 10 minutes. The ground state is depicted in Fig. 10 (c) and the photoexcited system in Fig. 10 (d): the apparent shift in energy, clearly visible in the k-integrated mode in Fig. 10 (b), is due to surface photovoltage (SPV).

The NB branch has also been used as a light source to study electron dynamics in Sr_2IrO_4.

These results have been presented in a conference [44] and will be detailed in a further publication.

The ARPES setup currently installed, a Phoibos 150 hemispherical analyzer by SPECS, provides also spin detection. A Very Low Energy Electron Diffraction (VLEED) spin polarimeter by Ferrum and a spin rotation lens system allow to probe the three-dimensional spin polarization of a photoelectron beam at a given kinetic energy and emission angle. The combination of this setup with the XUV-IR interferometer of the NB branch permits to study not only the charge but also the spin dynamics in photoemission (spin-, time- and angle-resolved photoemission spectroscopy, STARPES), as demonstrated in a proof-of-concept experiment realized on the Weyl Type-II semimetal WTe_2 [45].

4.3 BB branch

The BB branch mainly consists of two reflexions at close-to-normal incidence (86° angle) (Fig. 11). The first focusing mirror (CM) reflects the XUV and IR beams, the latter being a left over of the HHG process, to the second optical element of the branch which is a split mirror. It is made of two concentric plane mirrors. The central one (SM_{int}, 6 mm diameter) is specifically coated for XUV, while the external one (SM_{ext}) is silver coated for IR. SM_{int} is mounted on a piezo-actuated host so that the surfaces of the two mirrors can be shifted with nanometer precision to introduce a delay between the XUV and IR pulses. The base of the SM mount consists of a goniometer on top of a rotation stage (SmarAct) to adjust the global tip-tilt, and SM_{ext} is mounted on an independent tip-tilt mount to ajust the relative pointing.

After the HHG process, the central part of the beam passes through a 4 mm diameter, 200 nm thick aluminium filter, removing the IR beam almost completely within this radius. The external part is pure IR due to the lowest divergence of the XUV. Therefore only XUV is reflected on SM_{int} and only IR is reflected on SM_{ext}. The intensity of the IR pulse transmitted by the system is controlled with irises placed after the HHG source.

The compactness of this interferometric design ensures a high passive stability (Table 1) of the pump-probe delay [46]. Finally, since the optical system for CM can host two different mirrors,

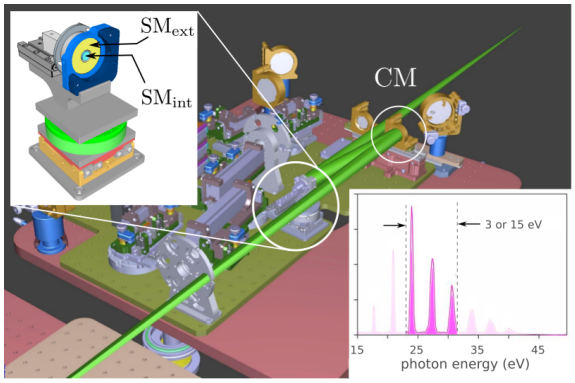

Fig. 11 The BB branch optical scheme. CM: curved mirror, SM: split mirror. Inset: typical spectrum transmitted by the system.

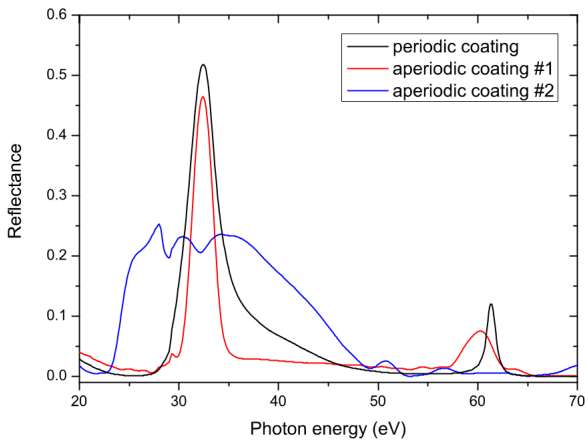

Fig. 12 Theoretical reflectance of Al/Sc/SiC coatings optimized for peak reflectance around 32.5 eV. The periodic one is represented for comparison but has not been deposited. The aperiodic coatings #1 (3 eV bandwidth) and #2 (15 eV bandwidth) are deposited in two sets of mirrors to be mounted as CM and SM_{int}.

it allows one to switch between different coatings, and hence to change the bandwidth of the transmitted light without disturbing any other parameter of the experiment. Specific coatings have been designed to preserve the shortest temporal duration of the pulses [47], and select either one or five consecutive harmonics from the initial emission.

4.3.1 Coatings design

Two specific multilayer interference coatings have been designed and developed at Laboratoire Charles Fabry with peak reflectance centered at

H21 (photon energy about 32.5 eV). These multilayer coatings are based on a combination of 3 materials: Al, Sc and SiC. We have shown previously that Al/Sc-based multilayers provide high theoretical efficiency in the wavelength ranging from 17 nm to 65 nm [48]. Al/Sc-based multilayer mirrors benefit from the presence of Al $L_{2,3}$ and Sc $M_{2,3}$ absorption edges, respectively at about 72 eV and 28 eV, and also from the increase of reflectance due to the 3 -material effect [49]. Moreover, we have recently achieved an experimental record of reflectance close to the Sc edge with periodic Al/Sc/SiC multilayers [50, 51]. The 4° angle of incidence on the mirrors was used for designing the coatings.

A first coating formula (#1) was optimized to obtain a bandwidth of less than 3 eV, in order to reflect efficiently H21 and suppress the other harmonics of the source. We have optimized an aperiodic Al/Sc/SiC stack by using TFCalc software in order to reach maximum reflectance at H21 and minimum reflectance for all other harmonics in the source spectrum. The coating contains 38 layers with individual thickness in the range 2 nm - 15 nm. The result of the optimization is shown on Fig. 12. We have also plotted the reflectance of an optimized periodic Al/Sc/SiC multilayer for comparison. Note that the aperiodic coating provides a reflectance higher than 45 % for H21 and allows one to reduce significantly the out-of-band reflectance.

A second coating formula (#2) was optimized with a broader bandwidth in order to reflects H17 to H25. The aperiodic Al/Sc/SiC stack contains layers with individual thickness ranging from 3 to 15 nm.

The two coatings have been deposited on 2 mirrors of BB branch (CM and SM_{int}) by magnetron sputtering. The deposition machine, Plassys MP800, consists of a 4-target RF/DC sputtering system and has been described in previous publication [49]. The deposition parameters are given in Ref. [51]. The coatings were characterized after the depostion by means of a grazing-incidence X-ray reflectometer (Bruker Discover D8) equipped with a Cu Kα radiation source.

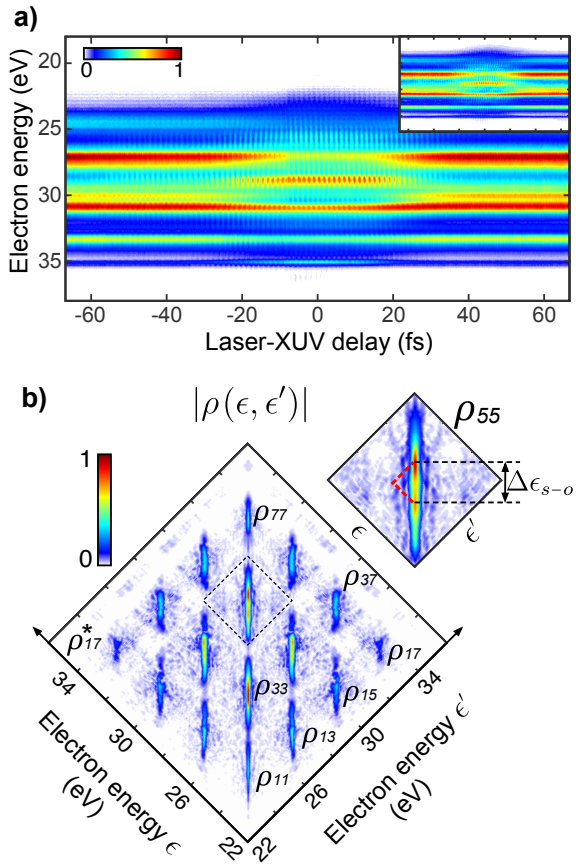

Fig. 13 a) Spectrogram measured on FAB10. Inset: spectrogram retrieved by the Mixed-FROG algorithm. b) Electron density matrix $\rho(\epsilon,\epsilon')$ (only modulus shown) reconstructed by the algorithm from the trace in a). Inset: Enlargement of the term ρ_{55} delimited by the black dashed square in the main panel.

4.3.2 Application of the BB branch: Mixed-FROG

To illustrate the capabilities of the BB branch and characterize thoroughtly the XUV emission, we present a Mixed-FROG measurement in Fig. 13 [34]. Similarly to approaches such as RABBIT [27] and streaking [52], this technique relies on laser-dressed photoelectron spectroscopy. It requires the measurement of a spectrogram, that is a trace representing the evolution of the photoelectron kinetic energy spectrum as a function of the laser-XUV delay. However, while other approaches assume a fully coherent ionization process, Mixed-FROG reconstructs a photoelectron

density matrix $\rho(\epsilon, \epsilon')$ giving access to the incoherent contributions of classical phenomena (shot-to-shot fluctuations, delay instabilities, space-time couplings...) [53] and quantum phenomena (entanglement of the photoelectron with unresolved degrees of freedom) [54]. In practice, the spectrogram needs to be processed with an iterative algorithm that extracts the quantum interferences between electron energy states and builds up the quantity $\rho(\epsilon, \epsilon')$.

For the measurement detailed in Fig. 13, harmonics H17 to H23 were isolated with the selective multilayer coatings (aperiodic coating #2, Fig. 12). Krypton was used as the generation and detection gas in the sensitive region of the TOF spectrometer. Due to spin-orbit coupling, photoionization can occur through two channels separated in energy by $\Delta\epsilon_{s-o} = 0.67\,\text{eV}$. The laser-XUV delay was scanned by steps of 67 as. 2001 photoelectron spectra were collected in order to form the spectrogram shown in Fig. 13 (a). An accelerating voltage of 12 V was used in the drift tube of the TOF. This trace was then processed with the difference map algorithm described in Ref. [34] using 40 modes and 400 iterations (see the retrieved spectrogram in the inset Fig. 13 (a)). The reconstructed electron density matrix is shown in Fig. 13 (b).

Along the matrix's diagonal (the vertical axis in the figure), the terms ρ_{11} to ρ_{77} correspond to the four energy levels, labeled 1, 3, 5 and 7, populated by the four high harmonics, whereas the off-diagonal elements, e.g. ρ_{13}, represent the coherences and indicate the ability for two levels to interfere with each other. All the terms exhibit a typical elongation along the diagonal, which was previously attributed to the limited resolution of the TOF spectrometer [34]. More precisely the diagonal terms $\rho(\epsilon, \epsilon)$ correspond to the experimentally detected dressing-free photoelectron spectrum which is incoherently broadened by the detector. Oppositely, along the antidiagonal axis the narrowband signal provides the spectral width populated coherently by the harmonics.

Moreover two maxima separated by $\Delta\epsilon_{s-o}$ are particularly visible in ρ_{55}, see the inset of Fig. 13 (b). This shows that the continuum is populated through the two ionization channels associated to spin-orbit coupling. However no corresponding off-diagonal term can be seen at the intersection of the red dashed lines in the inset, which seems to indicate that the two spin-orbit channels contribute incoherently to the ionization process [55]. These preliminary results will need to be confirmed by a thorough upcoming experimental study.

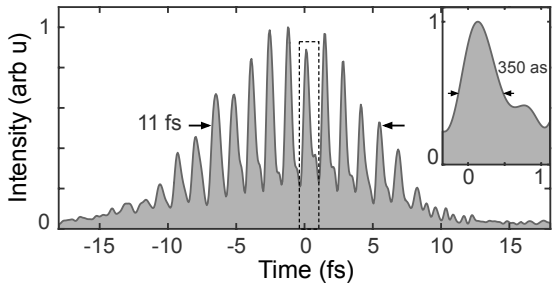

Fig. 14 Temporal intensity profile of the ensemble-averaged electron wavepacket obtained after performing a Fourier transform of $\rho(\epsilon, \epsilon')$. Inset: Enlargement of the area delimited by the black dashed rectangle in the main panel.

Finally Fourier-transforming $\rho(\epsilon, \epsilon')$ provides time-domain information [34], especially the temporal intensity profile of the ensemble-averaged electron wavepacket is shown in Fig. 14. Its shape is mostly dictated by that of the ionizing XUV attosecond pulse train. Especially its full-width-at-half-maximum duration of 11 fs is consistent with the expected duration of the 25 fs laser pulse driving the HHG process. The isolated pulses duration of 350 as corresponds to the width of the statistical ensemble of the attosecond pulses. It thus includes a possible pump-probe delay jitter.

4.4 VBB branch

The VBB branch is designed to be as achromatic as possible, using two grazing incidence (8° angle) reflections on gold coated mirrors, one flat and one toroidal. The optical setup is shown in Fig. 15. The flat mirror was originally designed as a two part mirror for a tight delay control, as for the BB beamline. However, designing such a mirror at grazing angle adds great mechanical complexity and the implementation of this feature was finally postponed.

In the current implementation, the recombination of the IR beam is done on a 3 mm diameter drilled mirror (orange path Fig. 15). As we suspect that the heating of the in-vacuum mirrors by the IR is one of the main source of the interferometer drift, broadband dielectric mirrors are used to transport the beam to limit absorption.

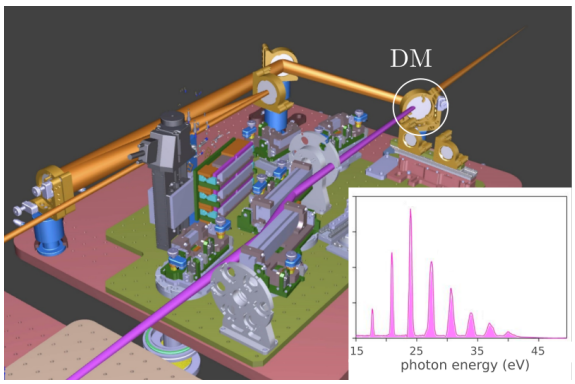

Fig. 15 The VBB branch optical scheme. DM: drilled mirror. Inset: typical spectrum transmitted by the system.

The LIZARD active stabilization technique

The interferometric stability of this branch is particularly important since it is intended to address experiments that need subfemtosecond pump-probe stability over hours of acquisition time. An original technique has been developed during the commissioning of the beamline to perform an *in-situ* active stabilization of the pump-probe delay by the use of the electronic signal from the magnetic bottle. The LIZARD technique allows one to control the delay between an XUV ATP and a dressing IR femtosecond pulse with attosecond precision. The error signal needed for the feedback is constructed by analysing, in an electron spectrometer, the oscillations with the time delay of two ionization channels that occur in such conditions [25]. The application of the technique will be illustrated in the next section.

4.4.1 Application of the VBB branch

Angularly resolved photoionization time-delays

In this section we present angle-resolved photoemission time-delays results in argon obtained with the actively-stabilized interferometer in the VBB branch [25]. Photoelectrons corresponding to the ionization of the $3p$ shell of argon with XUV + IR pulses are collected in the Velocity Map Imaging Spectrometer (VMIS) described in Ref. [56]. Previous angle-resolved RABBIT experiments with a COLTRIMS type apparatus have been performed on the FAB10 beamline [35], however without active stabilization of the XUV-IR delay. The experiments of Ref. [35] therefore required gathering and coherently adding few tens of independent measurements, corresponding to an overall acquisition time of 14 hours. This difficulty drove the development of the LIZARD stabilization technique, now available. Here, the active stabilization allows the measurement of a photoelectron image at a given time delay for several minutes, and the results shown have been obtained in a total of 75 minutes. Figure 16 (top) displays a typical photoelectron image for argon ionized with harmonics H11-H21 in the presence of a dressing IR pulse. The maximum kinetic energy of the electrons is 11.2 eV. The electron wavepackets produced by ionization with harmonic H_{2q+1} and stimulated emission of one IR photon interfere with the ones originating from ionization with H_{2q-1} and absorption of one IR photon, giving rise to the so-called sideband SB_{2q} [27]. Each sideband signal amplitude and angular distribution oscillates with the XUV-IR delay, carrying information about the two-photon transition matrix elements.

For each XUV-IR time-delay, the photoelectron image is Abel-inverted with the pBASEX algorithm [57]. Its decomposition on Legendre polynomials is analyzed following the formalism in [35] to yield the angular variations of atomic time delays with respect to $\theta = 0°$ shown in Fig. 16 (Bottom). For each sideband, the atomic delay decreases with the emission angle. The angular dependency of atomic time delays is due to the asymmetry of absorption and emission in the interfering quantum pathways leading to the sideband [58]. Due to the presence of an intermediate resonance excited by H17, the results for SB16 are strongly dependent on the exact photon energy [59]. The results for SB14 are in very good agreement with Refs. [35, 59]. These measurements demonstrate the ability of the VBB branch of the beamline to perform actively-stabilized attosecond measurements in a user end station. This opens the way to attosecond electron interferometry experiments in more complex systems.

RABBIT on solids

The combination of a sufficiently high repetition rate of 10 kHz and the LIZARD active stablization technique allows to probe attosecond photoemission time delays not only from gas systems but also from solid state targets. The RABBIT technique in condensed matter has been proven to give access to relative time delays between different

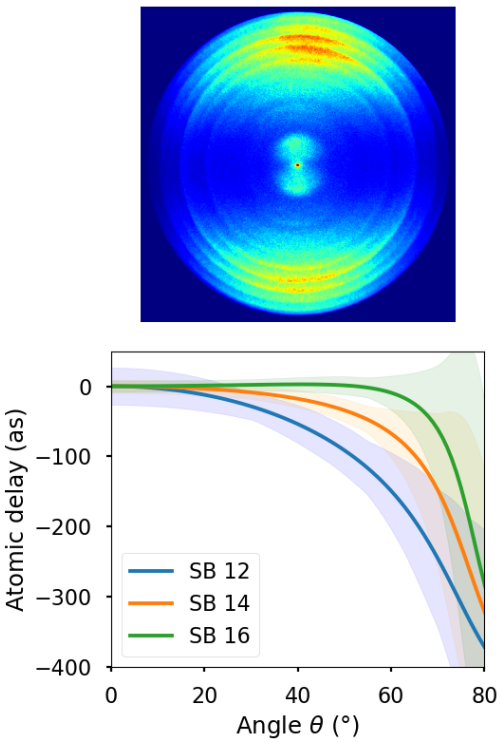

Fig. 16 (Top) Typical photoelectron image in argon acquired over 90 s at a given XUV-IR delay. Both lasers polarization are vertical. (Bottom) Angle dependence of the atomic delay for sidebands 12, 14 and 16. The angle θ is defined with respect to the light polarization axis. The shaded area correspond to the uncertainty as defined in [60].

initial states [61, 62], final states [63], geometries [64] and materials [65, 66]. Despite the success of these results, RABBIT on solids remains a complex technique of difficult access, limited among other effects by the important space charge on the solid surface from secondary electrons generated by the IR dressing [67].

A Phoibos 150 hemispherical analyzer by SPECS for angle-resolved photoemission spectroscopy (ARPES) experiments is currently installed at the FAB10 beamline. Very recently, we commissioned this setup on the VBB branch by using a target of Au(111) single crystal, and we defined the following procedure in order to prepare a RABBIT scan.

The alignment of the experimental chamber and the centering of the beam on the sample

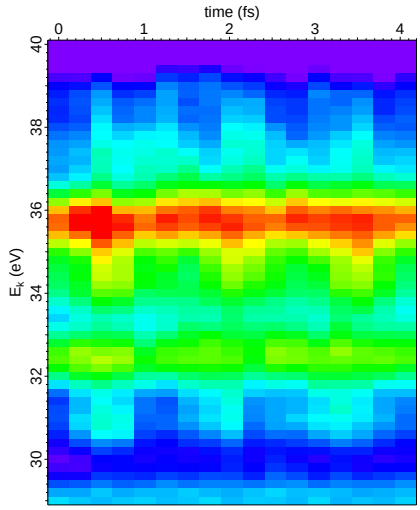

Fig. 17 RABBIT scan on Au(111). For each time delay, data are normalized by the total count of electrons in the measured energy and angular windows, and by the transmission function of the detector. For a given energy, the signal oscillates with a period of 1.33 fs, which is twice the period of the laser driver, as expected for a RABBIT trace. The 17 delay steps are separated by 254 as, thus the delay scan shown here covers three periods of oscillation. The accumulation time for each delay step was of 4.5 min. The delay range has been scanned three times, and the figure presents the average of those scans without any further post-treatment for readjustment of the delays. The full acquisition time is thus of 230 min.

placed at the analyzer focus is done by maximizing the transmission of photoelectrons through the analyzer slit. The Au surface was prepared by several sputtering and annealing cycles, and its quality has been validated by the observation of the well-known metallic parabolic surface state in ARPES mode measured with a helium lamp. However, the generation of secondary electrons by the intense IR dressing beam is still extremely dependent on the sample position, varying by more than 3 orders of magnitude with steps of less than a few hundreds micrometers. The sample position was optimized in order to minimize the secondary electrons emitted by the IR dressing field, finding about 1000 counts per second at 30 eV of kinetic energy with 6 μJ per IR pulse, which corresponds to a few percents of the signal from the XUV pulse only. The HHG conditions are then optimized by maximizing the contrast of peaks in the photoemission spectra. Finally, we make sure that the intensity of photoelectrons with XUV and IR together is comparable to the

sum of the photoelectron counts with the two beams independently. Under these conditions, we increase the XUV intensity as much as possible without important deformation of the spectrum due to space charge except for an energy offset. For Au(111) we find that an energy of about 15 pJ per pulse is a good compromise. We observe an energy offset of the spectrum of about 6 eV, of the order of what is estimated by the model in Ref. [43]. A RABBIT trace is measured by scanning the XUV-IR delay, actively stabilized by the LIZARD technique. For each time point, angle-resolved photoemission spectra are measured by sweeping the kinetic energy window several times, in order to average low frequency fluctuations of the XUV intensity. If more traces are measured under stable conditions, they can be summed to increase the signal to noise ratio.

In Fig. 17 the first RABBIT trace on Au(111) obtained at FAB10 is shown. The crystal is oriented with the ΓK direction at 10° from the analyzer slit. The XUV and IR beams are p-polarized. In the kinetic energy window shown, harmonics 17 and 19 excite the *d* band manifold of Au, resulting in broad peaks at 32.6 and 35.7 eV. Corresponding sidebands are observed on both the high- and low-energy sides of the peaks. The image shown corresponds to an energy distribution curve (EDC) integrated for $7.5 \pm 1°$ of emission angle, but the whole angular range of $\pm 15°$ is also recorded. Data will be analyzed and published in a future publication.

5 CONCLUSION AND PERSPECTIVES

We presented the performances of FAB10 and illustrated its capabilities with different commissioning experiments in gas and condensed phases. The beamline is a meeting point for numerous scientific communities and thus provides a rich and diverse environment that favours the emergence of new ideas. In a future upgrade, we will implement a modification of our hemispherical analyser to allow studies in the gas phase and benefit from its high spectral resolution compared to the TOF electron spectrometer. This implementation could be of great benefit for Mixed-FROG analysis [34] and future studies of decoherence of ultrafast electron wavepackets.

Further developments will implement a post-compression stage based on a multipass cell [68, 69], with an adaptation of the LIZARD technique to isolated attosecond pulses [70]. Moreover, the XUV source will be improved by implementing microfluidic glass cell technology [71]. The production of XUV circularly polarized light should also be implemented in the future. On a longer time scale, future upgrades of the laser source will most likely be aimed at achieving higher repetition rates.

Among the several results obtained on the beamline, the most recent one was the observation of a RABBIT signal on a solid target (Fig. 17), which opens particularly enticing new perspectives. In future studies, we plan to explore spin-dependent photoemission time delays, which have very rarely been observed so far. It will be particularly interesting to compare those measurements with those of static spin-resolved ARPES [72]. This project will fully exploit the numerous capabilities of the beamline, namely the XUV spectral filter, the active stabilization of the pump-probe delay, and the photoelectron spin resolution.

6 ACKNOWLEDGMENTS

We dedicate this article to the memory of our esteemed colleague and friend Bertrand Carré, whose visionary insight into attosecond science led to the construction of the ATTOLab facility, and to the design of the FAB10 beamline.

This research was supported by Agence Nationale de la Recherche, grant nos. ANR-11-EQPX0005-ATTOLAB, ANR-20-CE30-0007-02-DECAP, ANR-14-CE32-0010–XSTASE, and ANR-10-LABX-0039-PALM; Région Ile de France SESAME-2015-Pulse-X and SESAME-2012-ATTOLITE; Université Paris-Saclay LIDEX-2014-OPT2X ; and Laserlab-Europe EU-H2020-871124.

References

[1] Ferray, M., L'Huillier, A., Li, X.F., Mainfray, G., Manus, C.: Multiple-harmonic conversion of 1064 nm radiation in rare gases. J. Phys. B **21**, 31 (1988). https://doi.org/10.1088/0953-4075/21/3/001

[2] McPherson, A., Gibson, G., Jara, H., Johann, U., Luk, T.S., McIntyre, I.A., Boyer, K., Rhodes, C.K.: Studies of multiphoton production of vacuum-ultraviolet radiation in the rare gases. J. Opt. Soc. Am. B **4**(4), 595–601 (1987). https://doi.org/10.1364/JOSAB.4.000595

[3] Holldack, K., Bahrdt, J., Balzer, A., Bovensiepen, U., Brzhezinskaya, M., Erko, A., Eschenlohr, A., Follath, R., Firsov, A., Frentrup, W., Le Guyader, L., Kachel, T., Kuske, P., Mitzner, R., Müller, R., Pontius, N., Quast, T., Radu, I., Schmidt, J.-S., Schüßler-Langeheine, C., Sperling, M., Stamm, C., Trabant, C., Föhlisch, A.: FemtoSpeX: a versatile optical pump–soft X-ray probe facility with 100fs X-ray pulses of variable polarization. Journal of Synchrotron Radiation **21**(5), 1090–1104 (2014). https://doi.org/10.1107/S1600577514012247

[4] Prigent, P., Hollander, P., Labat, M., Couprie, M.E., Marlats, J.L., Laulhé, C., Luning, J., Moreno, T., Morin, P., Nadji, A., Polack, F., Ravy, S., Silly, M., Sirotti, F.: Progress on the Femto-Slicing Project at the Synchrotron SOLEIL. Journal of Physics: Conference Series **425**(7), 072022 (2013). https://doi.org/10.1088/1742-6596/425/7/072022

[5] Silly, M.G., Ferté, T., Tordeux, M.A., Pierucci, D., Beaulieu, N., Chauvet, C., Pressacco, F., Sirotti, F., Popescu, H., Lopez-Flores, V., Tortarolo, M., Sacchi, M., Jaouen, N., Hollander, P., Ricaud, J.P., Bergeard, N., Boeglin, C., Tudu, B., Delaunay, R., Luning, J., Malinowski, G., Hehn, M., Baumier, C., Fortuna, F., Krizmancic, D., Stebel, L., Sergo, R., Cautero, G.: Pump−probe experiments at the TEMPO beamline using the low-α operation mode of Synchrotron SOLEIL. Journal of Synchrotron Radiation **24**(4), 886–897 (2017). https://doi.org/10.1107/S1600577517007913

[6] Maroju, P.K., Grazioli, C., Fraia, M.D., Moioli, M., Ertel, D., Ahmadi, H., Plekan, O., Finetti, P., Allaria, E., Giannessi, L., Ninno, G.D., Spezzani, C., Penco, G., Spampinati, S., Demidovich, A., Danailov, M.B., Borghes, R., Kourousias, G., Reis, C.E.S.D., Billé, F., Lutman, A.A., Squibb, R.J., Feifel, R., Carpeggiani, P., Reduzzi, M., Mazza, T., Meyer, M., Bengtsson, S., Ibrakovic, N., Simpson, E.R., Mauritsson, J., Csizmadia, T., Dumergue, M., Kühn, S., Gopalakrishna, H.N., You, D., Ueda, K., Labeye, M., Bækhøj, J.E., Schafer, K.J., Gryzlova, E.V., Grum-Grzhimailo, A.N., Prince, K.C., Callegari, C., Sansone, G.: Attosecond pulse shaping using a seeded free-electron laser. Nature **578**(7795), 386–391 (2020). https://doi.org/10.1038/s41586-020-2005-6

[7] Haynes, D.C., Wurzer, M., Schletter, A., Al-Haddad, A., Blaga, C., Bostedt, C., Bozek, J., Bromberger, H., Bucher, M., Camper, A., Carron, S., Coffee, R., Costello, J.T., DiMauro, L.F., Ding, Y., Ferguson, K., Grguraš, I., Helml, W., Hoffmann, M.C., Ilchen, M., Jalas, S., Kabachnik, N.M., Kazansky, A.K., Kienberger, R., Maier, A.R., Maxwell, T., Mazza, T., Meyer, M., Park, H., Robinson, J., Roedig, C., Schlarb, H., Singla, R., Tellkamp, F., Walker, P.A., Zhang, K., Doumy, G., Behrens, C., Cavalieri, A.L.: Clocking auger electrons. Nature Physics **17**(4), 512–518 (2021). https://doi.org/10.1038/s41567-020-01111-0

[8] Duris, J., Li, S., Driver, T., Champenois, E.G., MacArthur, J.P., Lutman, A.A., Zhang, Z., Rosenberger, P., Aldrich, J.W., Coffee, R., Coslovich, G., Decker, F.-J., Glownia, J.M., Hartmann, G., Helml, W., Kamalov, A., Knurr, J., Krzywinski, J., Lin, M.-F., Marangos, J.P., Nantel, M., Natan, A., O'Neal, J.T., Shivaram, N., Walter, P., Wang, A.L., Welch, J.J., Wolf, T.J.A., Xu, J.Z., Kling, M.F., Bucksbaum, P.H., Zholents, A., Huang, Z., Cryan, J.P., Marinelli, A.: Tunable isolated attosecond X-ray pulses with gigawatt peak power from a free-electron laser. Nature Photonics **14**(1), 30–36 (2020). https://doi.org/10.1038/s41566-019-0549-5

[9] Mandal, A., Sidhu, M.S., Rost, J.M., Pfeifer, T., Singh, K.P.: Attosecond delay lines: design, characterization and applications. The European Physical Journal Special Topics **230**(23), 4195–4213 (2021). https://doi.

org/10.1140/epjs/s11734-021-00261-3

[10] Kühn, S., Dumergue, M., Kahaly, S., Mondal, S., Füle, M., Csizmadia, T., Farkas, B., Major, B., Várallyay, Z., Cormier, E., Kalashnikov, M., Calegari, F., Devetta, M., Frassetto, F., Månsson, E., Poletto, L., Stagira, S., Vozzi, C., Nisoli, M., Rudawski, P., Maclot, S., Campi, F., Wikmark, H., Arnold, C.L., Heyl, C.M., Johnsson, P., L'Huillier, A., Lopez-Martens, R., Haessler, S., Bocoum, M., Boehle, F., Vernier, A., Iaquaniello, G., Skantzakis, E., Papadakis, N., Kalpouzos, C., Tzallas, P., Lépine, F., Charalambidis, D., Varjú, K., Osvay, K., Sansone, G.: The ELI-ALPS facility: the next generation of attosecond sources. Journal of Physics B: Atomic, Molecular and Optical Physics **50**(13), 132002 (2017). https://doi.org/10.1088/1361-6455/aa6ee8

[11] Turcu, I.C.E., Springate, E., Froud, C.A., Cacho, C.M., Collier, J.L., Bryan, W.A., Nemeth, G.R.A.J., Marangos, J.P., Tisch, J.W.G., Torres, R., Siegel, T., Brugnera, L., Underwood, J.G., Procino, I., Newell, W.R., Altucci, C., Velotta, R., King, R.B., Alexander, J.D., Calvert, C.R., Kelly, O., Greenwood, J.B., Williams, I.D., Cavalleri, A., Petersen, J.C., Dean, N., Dhesi, S.S., Poletto, L., Villoresi, P., Frassetto, F., Bonora, S., Roper, M.D.: Ultrafast science and development at the Artemis facility **7469**, 746902 (2010). https://doi.org/10.1117/12.867540

[12] Strickland, D., Mourou, G.: Compression of amplified chirped optical pulses. Opt. Commun. **56**, 219 (1985). https://doi.org/10.1016/0030-4018(85)90151-8

[13] Koke, S., Grebing, C., Frei, H., Anderson, A., Assion, A., Steinmeyer, G.: Direct frequency comb synthesis with arbitrary offset and shot-noise-limited phase noise. Nature Photonics **4**(7), 462–465 (2010). https://doi.org/10.1038/nphoton.2010.91

[14] Cheriaux, G., Rousseau, P., Salin, F., Chambaret, J.P., Walker, B., Dimauro, L.F.: Aberration-free stretcher design for ultrashort-pulse amplification. Optics Letters **21**(6), 414–416 (1996). https://doi.org/10.1364/OL.21.000414

[15] Hergott, J.-F., Tcherbakoff, O., Paul, P.-M., Demengeot, P., Perdrix, M., Lepetit, F., Garzella, D., Guillaumet, D., Comte, M., Oliveira, P.D., Gobert, O.: Carrier-Envelope Phase stabilization of a 20 W, grating based, chirped-pulse amplified laser, using Electro-Optic effect in a $LiNbO_3$ crystal. Optics Express **19**(21), 19935–19941 (2011). https://doi.org/10.1364/OE.19.019935

[16] Verluise, F., Laude, V., Cheng, Z., Spielmann, C., Tournois, P.: Amplitude and phase control of ultrashort pulses by use of an acousto-optic programmable dispersive filter: pulse compression and shaping. Optics Letters **25**(8), 575–577 (2000). https://doi.org/10.1364/OL.25.000575

[17] Golinelli, A., Chen, X., Gontier, E., Bussière, B., Tcherbakoff, O., Natile, M., D'Oliveira, P., Paul, P.-M., Hergott, J.-F.: Original Ti:Sa 10 kHz front-end design delivering 17 fs, 170 mrad CEP stabilized pulses up to 5 W. Opt. Lett. **42**(12), 2326–2329 (2017). https://doi.org/10.1364/OL.42.002326

[18] Hotz, D.F.: Gain Narrowing in a Laser Amplifier. Applied Optics **4**(5), 527–530 (1965). https://doi.org/10.1364/AO.4.000527

[19] Oksenhendler, T., Kaplan, D., Tournois, P., Greetham, G.M., Estable, F.: Intracavity acousto-optic programmable gain control for ultra-wide-band regenerative amplifiers. Applied Physics B **83**(4), 491 (2006). https://doi.org/10.1007/s00340-006-2231-0

[20] Golinelli, A., Chen, X., Bussière, B., Gontier, E., Paul, P.-M., Tcherbakoff, O., D'Oliveira, P., Hergott, J.-F.: CEP-stabilized, sub-18 fs, 10 kHz and TW-class 1 kHz dual output Ti:Sa laser with wavelength tunability option. Optics Express **27**(10), 13624–13636 (2019). https://doi.org/10.1364/OE.27.013624

[21] Feng, C., Hergott, J.-F., Paul, P.-M., Chen, X., Tcherbakoff, O., Comte, M., Gobert, O., Reduzzi, M., Calegari, F., Manzoni, C., Nisoli, M., Sansone, G.: Complete analog

control of the carrier-envelope-phase of a high-power laser amplifier. Optics Express **21**(21), 25248–25256 (2013). https://doi.org/10.1364/OE.21.025248

[22] Squier, J., Barty, C.P.J., Salin, F., Blanc, C.L., Kane, S.: Use of mismatched grating pairs in chirped-pulse amplification systems. Applied Optics **37**(9), 1638–1641 (1998). https://doi.org/10.1364/AO.37.001638

[23] Weber, S.J., Manschwetus, B., Billon, M., Böttcher, M., Bougeard, M., Breger, P., Géléoc, M., Gruson, V., Huetz, A., Lin, N., Picard, Y.J., Ruchon, T., Salières, P., Carré, B.: Flexible attosecond beamline for high harmonic spectroscopy and xuv/near-ir pump probe experiments requiring long acquisition times. Review of Scientific Instruments **86**(3) (2015). https://doi.org/10.1063/1.4914464

[24] Alexandridi, C., Platzer, D., Barreau, L., Busto, D., Zhong, S., Turconi, M., Neoričić, L., Laurell, H., Arnold, C.L., Borot, A., Hergott, J.-F., Tcherbakoff, O., Lejman, M., Gisselbrecht, M., Lindroth, E., L'Huillier, A., Dahlström, J.M., Salières, P.: Attosecond photoionization dynamics in the vicinity of the Cooper minima in argon. Physical Review Research **3**(1), 012012 (2021). https://doi.org/10.1103/PhysRevResearch.3.L012012

[25] Luttmann, M., Bresteau, D., Hergott, J.-F., Tcherbakoff, O., Ruchon, T.: In situ sub-50-attosecond active stabilization of the delay between infrared and extreme-ultraviolet light pulses. Physical Review Applied **15**(3) (2021). https://doi.org/10.1103/physrevapplied.15.034036

[26] https://www.smaract.com/index-en. https://www.smaract.com/index-en

[27] Paul, P.M., Toma, E.S., Breger, P., Mullot, G., Augé, F., Balcou, P., Muller, H.G., Agostini, P.: Observation of a Train of Attosecond Pulses from High Harmonic Generation. Science **292**, 1689–1692 (2001). https://doi.org/10.1126/science.1059413

[28] Grazioli, C., Callegari, C., Ciavardini, A., Coreno, M., Frassetto, F., Gauthier, D., Golob, D., Ivanov, R., Kivimäki, A., Mahieu, B., Bučar, B., Merhar, M., Miotti, P., Poletto, L., Polo, E., Ressel, B., Spezzani, C., De Ninno, G.: CITIUS: An infrared-extreme ultraviolet light source for fundamental and applied ultrafast science. Review of Scientific Instruments **85**(2), 23104 (2014). https://doi.org/10.1063/1.4864298

[29] https://vuo.elettra.eu/services/elements/data/au.txt. https://vuo.elettra.eu/services/elements/data/au.txt

[30] Ye, P., Gulyás Oldal, L., Csizmadia, T., Filus, Z., Grósz, T., Jójárt, P., Seres, I., Bengery, Z., Gilicze, B., Kahaly, S., Varjú, K., Major, B.: High-Flux 100 kHz Attosecond Pulse Source Driven by a High-Average Power Annular Laser Beam. Ultrafast Science **2022** (2022). https://doi.org/10.34133/2022/9823783

[31] Artemis 1 kHz XUV beamline with monochromator. https://www.clf.stfc.ac.uk/Pages/XUV-beamlines.aspx

[32] https://www.crytur.com/

[33] Kruit, P., Read, F.H.: Magnetic field paralleliser for 2π electron-spectrometer and electron-image magnifier. J. Phys. E **16**, 313 (1983). https://doi.org/10.1088/0022-3735/16/4/016

[34] Bourassin-Bouchet, C., Barreau, L., Gruson, V., Hergott, J.-F., Quéré, F., Salières, P., Ruchon, T.: Quantifying decoherence in attosecond metrology. Physical Review X **10**(3) (2020). https://doi.org/10.1103/physrevx.10.031048

[35] Joseph, J., Holzmeier, F., Bresteau, D., Spezzani, C., Ruchon, T., Hergott, J.F., Tcherbakoff, O., D'Oliveira, P., Houver, J.C., Dowek, D.: Angle-resolved studies of XUV–IR two-photon ionization in the RABBITT scheme. Journal of Physics B: Atomic, Molecular and Optical Physics **53**(18), 184007 (2020). https://doi.org/10.1088/1361-6455/ab9f0d

[36] Weber, S.J.: PyMoDAQ: An open-source Python-based software for modular data

acquisition. Review of Scientific Instruments **92**(4), 045104 (2021). https://doi.org/10.1063/5.0032116

[37] https://www.cinel.com/cinel/

[38] Senf, F., Flechsig, U., Eggenstein, F., Gudat, W., Klein, R., Rabus, H., Ulm, G.: A plane-grating monochromator beamline for the PTB undulators at BESSY II. Journal of Synchrotron Radiation **5**(3), 780–782 (1998). https://doi.org/10.1107/S0909049597020323

[39] Petersen, H., Jung, C., Hellwig, C., Peatman, W.B., Gudat, W.: Review of plane grating focusing for soft x-ray monochromators. Review of Scientific Instruments **66**(1), 1–14 (1995). https://doi.org/10.1063/1.1145258

[40] Frassetto, F., Cacho, C., Froud, C.A., Turcu, I.C.E., Villoresi, P., Bryan, W.A., Springate, E., Poletto, L.: Single-grating monochromator for extreme-ultraviolet ultrashort pulses. Opt. Express **19**(20), 19169–19181 (2011). https://doi.org/10.1364/OE.19.019169

[41] The Abbe condition states that the coma aberration can be limited when the sines of incoming and outgoing beams change proportionally in the aperture of the system.

[42] Poletto, L., Frassetto, F.: Time-preserving grating monochromators for ultrafast extreme-ultraviolet pulses. Appl. Opt. **49**(28), 5465–5473 (2010). https://doi.org/10.1364/AO.49.005465

[43] Corder, C., Zhao, P., Bakalis, J., Li, X., Kershis, M.D., Muraca, A.R., White, M.G., Allison, T.K.: Ultrafast extreme ultraviolet photoemission without space charge. Structural Dynamics **5**(5), 054301 (2018). https://doi.org/10.1063/1.5045578

[44] Caillaux, J., Bresteau, D., Ruchon, T., Cilento, F., Parmigiani, F., Vadillotorre, I., Spezzani, C., Tcherbakoff, O., D'Oliveira, P., Salière, P., Polack, F., Dennetiere, D., Brouet, V., Marsi, M.: Ultrafast electron dynamics in strontium iridate (Conference Presentation) **11346** (2020). https://doi.org/10.1117/12.2555039

[45] Fanciulli, M., Schusser, J., Lee, M.-I., Youbi, Z.E., Heckmann, O., Richter, M.C., Cacho, C., Spezzani, C., Bresteau, D., Hergott, J.-F.m.c., D'Oliveira, P., Tcherbakoff, O., Ruchon, T., Minár, J., Hricovini, K.: Spin, time, and angle resolved photoemission spectroscopy on WTe2. Phys. Rev. Research **2**, 013261 (2020). https://doi.org/10.1103/PhysRevResearch.2.013261

[46] Böttcher, F.M., Manschwetus, B., Rottke, H., Zhavoronkov, N., Ansari, Z., Sandner, W.: Interferometric long-term stabilization of a delay line: a tool for pump–probe photoelectron–photoion-coincidence spectroscopy on the attosecond time scale. Applied Physics B **91**(2), 287–293 (2008). https://doi.org/10.1007/s00340-008-2987-5

[47] Bourassin-Bouchet, C., de Rossi, S., Wang, J., Meltchakov, E., Giglia, A., Mahne, N., Nannarone, S., Delmotte, F.: Shaping of single-cycle sub-50-attosecond pulses with multilayer mirrors. New Journal of Physics **14**(2), 023040 (2012). https://doi.org/10.1088/1367-2630/14/2/023040

[48] Delmotte, F., Dehlinger, M., Bourassin-Bouchet, C., Rossi, S.d., Jerome, A., Meltchakov, E., Varnière, F.: Multilayer optics for coherent EUV/X-ray laser sources **9589**, 29–37 (2015). https://doi.org/10.1117/12.2188048

[49] Gautier, J., Delmotte, F., Roulliay, M., Bridou, F., Ravet, M.-F., Jérome, A.: Study of normal incidence of three-component multilayer mirrors in the range 20–40 nm. Applied Optics **44**(3), 384–390 (2005). https://doi.org/10.1364/AO.44.000384

[50] Rebellato, J., Soufli, R., Meltchakov, E., Gullikson, E., de Rossi, S., Delmotte, F.: High efficiency Al/Sc-based multilayer coatings in the EUV wavelength range above 40 nanometers. Optics letters **45**(4), 869–872 (2020). https://doi.org/10.1364/OL.384734

[51] Rebellato, J., Soufli, R., Meltchakov, E., Gullikson, E.M., de Rossi, S., Baumier, C., Pallier, F., Delmotte, F.: Optical, structural and aging properties of Al/Sc-based multilayers for the extreme ultraviolet. Thin Solid Films **735**, 138873 (2021). https://doi.org/10.1016/j.tsf.2021.138873

[52] Hentschel, M., Kienberger, R., Spielmann, C., Reider, G.A., Milosevic, N., Brabec, T., Corkum, P., Heinzmannß, U., Drescher, M., Krausz, F.: Attosecond metrology. Nature **414**, 509 (2001). https://doi.org/10.1038/35107000

[53] Bourassin-Bouchet, C., Couprie, M.-E.: Partially coherent ultrafast spectrography. Nature Communications **6**(1), 6465 (2015). https://doi.org/10.1038/ncomms7465

[54] Pabst, S., Greenman, L., Ho, P.J., Mazziotti, D.A., Santra, R.: Decoherence in Attosecond Photoionization. Phys. Rev. Lett. **106**(5), 053003 (2011). https://doi.org/10.1103/PhysRevLett.106.053003

[55] Carlström, S., Mauritsson, J., Schafer, K.J., L'Huillier, A., Gisselbrecht, M.: Quantum coherence in photo-ionisation with tailored XUV pulses. Journal of Physics B: Atomic, Molecular and Optical Physics **51**(1), 015201 (2017). https://doi.org/10.1088/1361-6455/aa96e7

[56] Lietard, A., Piani, G., Poisson, L., Soep, B., Mestdagh, J.-M., Aloïse, S., Perrier, A., Jacquemin, D., Takeshita, M.: Competitive direct vs. indirect photochromism dynamics of constrained inverse dithienylethene molecules. Physical Chemistry Chemical Physics **16**(40), 22262–22272 (2014). https://doi.org/10.1039/C4CP02310B

[57] Garcia, G.A., Nahon, L., Powis, I.: Two-dimensional charged particle image inversion using a polar basis function expansion. Review of Scientific Instruments **75**(11), 4989–4996 (2004). https://doi.org/10.1063/1.1807578

[58] Busto, D., Vinbladh, J., Zhong, S., Isinger, M., Nandi, S., Maclot, S., Johnsson, P., Gisselbrecht, M., L'Huillier, A., Lindroth, E., Dahlström, J.M.: Fano's propensity rule in angle-resolved attosecond pump-probe photoionization. Phys. Rev. Lett. **123**, 133201 (2019). https://doi.org/10.1103/PhysRevLett.123.133201

[59] Cirelli, C., Marante, C., Heuser, S., Petersson, C., Galán, Á.J., Argenti, L., Zhong, S., Busto, D., Isinger, M., Nandi, S., *et al.*: Anisotropic photoemission time delays close to a fano resonance. Nature communications **9**(1), 1–9 (2018). https://doi.org/10.1038/s41467-018-03009-1

[60] Autuori, A., Platzer, D., Lejman, M., Gallician, G., Maëder, L., Covolo, A., Bosse, L., Dalui, M., Bresteau, D., Hergott, J.-F., Tcherbakoff, O., Marroux, H.J.B., Loriot, V., Lépine, F., Poisson, L., Taïeb, R., Caillat, J., Salières, P.: Anisotropic dynamics of two-photon ionization: An attosecond movie of photoemission. Science Advances **8**(12), 7594 (2022). https://doi.org/10.1126/sciadv.abl7594

[61] Kasmi, L., Lucchini, M., Castiglioni, L., Kliuiev, P., Osterwalder, J., Hengsberger, M., Gallmann, L., Krüger, P., Keller, U.: Effective mass effect in attosecond electron transport. Optica **4**(12), 1492–1497 (2017). https://doi.org/10.1364/OPTICA.4.001492

[62] Heinrich, S., Saule, T., Högner, M., Cui, Y., Yakovlev, V.S., Pupeza, I., Kleineberg, U.: Attosecond intra-valence band dynamics and resonant-photoemission delays in W (110). Nature communications **12**(1), 1–10 (2021). https://doi.org/10.1038/s41467-021-23650-7

[63] Tao, Z., Chen, C., Szilvási, T., Keller, M., Mavrikakis, M., Kapteyn, H., Murnane, M.: Direct time-domain observation of attosecond final-state lifetimes in photoemission from solids. Science **353**(6294), 62–67 (2016). https://doi.org/10.1126/science.aaf6793

[64] Lucchini, M., Castiglioni, L., Kasmi, L., Kliuiev, P., Ludwig, A., Greif, M., Osterwalder, J., Hengsberger, M., Gallmann, L., Keller, U.: Light-matter interaction

at surfaces in the spatiotemporal limit of macroscopic models. Physical Review Letters **115**(13) (2015). https://doi.org/10.1103/physrevlett.115.137401

[65] Locher, R., Castiglioni, L., Lucchini, M., Greif, M., Gallmann, L., Osterwalder, J., Hengsberger, M., Keller, U.: Energy-dependent photoemission delays from noble metal surfaces by attosecond interferometry. Optica **2**(5), 405 (2015). https://doi.org/10.1364/optica.2.000405

[66] Chen, C., Tao, Z., Carr, A., Matyba, P., Szilvási, T., Emmerich, S., Piecuch, M., Keller, M., Zusin, D., Eich, S., Rollinger, M., You, W., Mathias, S., Thumm, U., Mavrikakis, M., Aeschlimann, M., Oppeneer, P.M., Kapteyn, H., Murnane, M.: Distinguishing attosecond electron-electron scattering and screening in transition metals. Proceedings of the National Academy of Sciences **114**(27), 5300–5307 (2017). https://doi.org/10.1073/pnas.1706466114

[67] Saathoff, G., Miaja-Avila, L., Aeschlimann, M., Murnane, M.M., Kapteyn, H.C.: Laser-assisted photoemission from surfaces. Physical Review A **77**(2), 022903 (2008). https://doi.org/10.1103/PhysRevA.77.022903

[68] Hanna, M., Guichard, F., Daher, N., Bournet, Q., Délen, X., Georges, P.: Nonlinear Optics in Multipass Cells. Laser & Photonics Reviews **15**(12), 2100220 (2021). https://doi.org/10.1002/lpor.202100220

[69] Daniault, L., Cheng, Z., Kaur, J., Hergott, J.-F., Réau, F., Tcherbakoff, O., Daher, N., Délen, X., Hanna, M., Lopez-Martens, R.: Single-stage few-cycle nonlinear compression of milliJoule energy Ti:Sa femtosecond pulses in a multipass cell. Optics Letters **46**(20), 5264–5267 (2021). https://doi.org/10.1364/OL.442707

[70] Luttmann, M., Bresteau, D., Ruchon, T.: Pump-Probe Delay Controlled by Laser-dressed Ionization with Isolated Attosecond Pulses **255** (2021). https://doi.org/10.1051/epjconf/202125513004

[71] Ciriolo, A.G., Vázquez, R.M., Tosa, V., Frezzotti, A., Crippa, G., Devetta, M., Faccialá, D., Frassetto, F., Poletto, L., Pusala, A., Vozzi, C., Osellame, R., Stagira, S.: High-order harmonic generation in a microfluidic glass device. Journal of Physics: Photonics **2**(2), 024005 (2020). https://doi.org/10.1088/2515-7647/ab7d81

[72] Fanciulli, M., Volfová, H., Muff, S., Braun, J., Ebert, H., Minár, J., Heinzmann, U., Dil, J.H.: Spin Polarization and Attosecond Time Delay in Photoemission from Spin Degenerate States of Solids. Physical Review Letters **118**(6), 067402 (2017). https://doi.org/10.1103/PhysRevLett.118.067402